J. Fluid Mech. (1977), *vol.* 82, *part* 4, *pp.* 767–793
Printed in Great Britain

Growth and equilibrium of short gravity waves in a wind-wave tank

By W. J. PLANT AND J. W. WRIGHT
Ocean Sciences Division, Naval Research Laboratory, Washington D.C. 20375

(Received 8 September 1976)

Temporal and spatial development of short gravity waves in a linear wind-wave tank has been measured for wind speeds up to 15 m/s using microwave Doppler spectrometry. Surface waves of wavelength 4·1 cm, 9·8 cm, 16·5 cm and 36 cm were observed as a function of fetch, wind speed and wind duration. The waves grew exponentially from inception until they were about 10 dB smaller than their maximum height, and the temporal growth and spectral transport (spatial growth) rates were about equal when the wave amplitude was sufficiently small. The amplitude of a short gravity wave of fixed wavelength was found to decrease substantially at winds, fetches or durations greater than those at which the short gravity wave was approximately the dominant wave; such phenomena are sometimes referred to as overshoot. The dominant short gravity wave was observed to reach a maximum amplitude which depended only on wavelength, showing that wave breaking induced by an augmented wind drift cannot be the primary limitation to the wave height. Waves travelling against the wind were observed for wavelengths of 9·8 cm, 16·5 cm and 36 cm and were shown to be generated by the air flow at low wind speeds.

Measured initial growth rates for 16·5 cm and 36 cm waves were greater than expected, suggesting the existence of a growth mechanism in addition to direct transfer from the wind via linear instability of the boundary-layer flow. Initial temporal growth rates and spectral transport rates were compared to yield an experimental determination of the magnitude of the sum of nonlinear interactions and dissipation in short gravity waves. If the steady-state energy input in the neighbourhood of the dominant wave occurs at the measured initial temporal growth rates, then most of the energy input is locally dissipated; relatively little is advected away. Calculated gravity–capillary nonlinear energy transfer rates match those determined from initial growth rates for 9·8 cm waves and the gravity–capillary wave interaction continues to be significant for waves as long as 16·5 cm. For longer waves the gravity–capillary interaction is too small to bring the short gravity wave to a steady state when it is the dominant wave of the wind-wave system.

1. Introduction

When wind blows across water, waves grow until a dynamic equilibrium is achieved between the wind, dissipation forces and interactions among the waves themselves. In such a steady state in a linear wave tank the spectrum of the wave system is sharply peaked at some dominant wavelength and as the fetch or wind speed increases, the dominant wave grows in amplitude and shifts to lower frequencies. The objective of

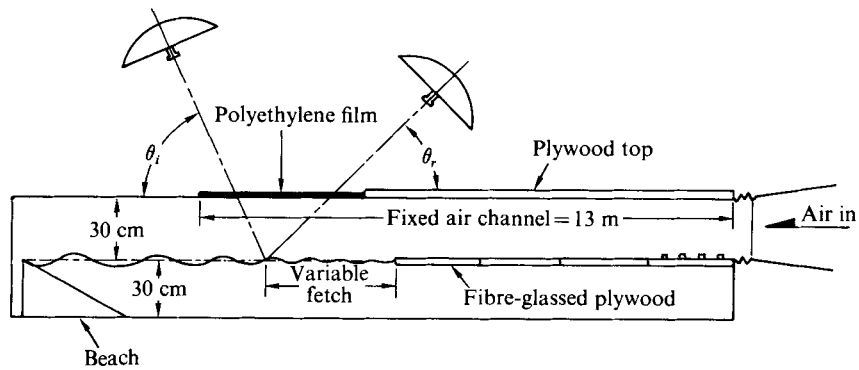

FIGURE 1. The microwave scattering geometry and wave-tank configuration (not to scale).

the experiments described in this paper was to study the temporal growth of these short gravity waves before they reach their steady state as well as the dependence of the steady-state waves on fetch and wind speed from their inception until they become somewhat shorter than the dominant wave of the system. Short gravity waves of wavelength 4·1 cm, 9·8 cm, 16·5 cm and 36 cm were selected. The principal measurement technique was microwave Doppler spectrometry using focused parabolic antennae, a technique discussed in some detail in the next section.

2. The parabolic antenna as a wave probe

The Doppler spectral measurements reported here were made in both backscatter and forward-scatter modes with parabolic antennae of diameter $D = 61$ cm and 143 cm and ratio of focal length to diameter of $\frac{1}{3}$. Focusing such an antenna (by changing the axial position of the feed) minimizes the curvature of the phase fronts at the focus. If the antenna is focused at the water surface and the range R to the surface is less than D^2/λ_0, where λ_0 is the microwavelength, then the surface is said to be under-illuminated; i.e. almost all the incident radiation is contained within the central Fresnel zone. In this sense the incident phase fronts are nearly planar. Now, if a uniform plane wave is incident on a plane surface slightly roughened by a surface displacement $\gamma(x, y, t)$, it is well known that the scattered power spectral density is proportional to the surface wave power spectral density F. That is, for incidence at a depression angle θ_i and reception at a depression angle θ_r as shown in figure 1, we have

$$\mathbf{k}_B = [k_0(\cos\theta_i - \cos\theta_r), 0] \tag{1}$$

and

$$P(k_0, \theta_i, \theta_r, \omega) \propto F(\mathbf{k}_B, \omega), \tag{2}$$

where $\mathbf{k}_B$ and k_0 are the Bragg wave vector and the microwavenumber respectively, P is the scattered power spectral density, and F is the surface displacement spectrum.

In the finite region illuminated by the parabolic antenna the relationship (2) is modified so that a small group of surface waves with wave vectors in the neighbourhood of $\mathbf{k}_B$ contribute. The effect can be described by a convolution of the power spectrum of the surface displacement with an antenna illumination function $V(k_x, k_y)$ (Larson & Wright 1974):

$$P(k_0, \theta_i, \theta_r, \omega) = f(\theta_1, \theta_r) \int F(\mathbf{k}, \omega)\, V(\mathbf{k}_B - \mathbf{k})\, d\mathbf{k}, \tag{3}$$

where $f(\theta_i, \theta_r)$ is a function also of the dielectric constant and polarization determinable from first-order scattering theory (Wright 1966). The resolution in wavenumber for the antenna used as a wave probe, which is determined by the antenna function V, is attributable to two effects. First, the residual curvature of the phase fronts is an important source of broadening (Wright & Keller 1971). Overillumination, i.e. irradiation of many Fresnel zones as in the far field, is not the best illumination for Bragg scattering measurements. Second, the finite size of the focused spot broadens V in an obvious way as does the, perhaps less obvious, influence of the longitudinal electromagnetic field which must exist owing to the restricted size of the focused spot. These fields, in addition to contributing to the broadening of V, also modify the function $f(\theta_i, \theta_r)$. Since we do not report on absolute values of the scattering cross-section, this modification is not of much concern to us here.

In the case of horn antennae, a form for V may be calculated (Wright & Keller 1971) which gives fair agreement with measured spectra. In fact, it is a good deal easier, and probably more accurate, to measure V using scattering by monochromatic water waves. In this case F is very narrow compared with V, and ω and k are uniquely related by the dispersion relation for gravity–capillary waves. This is well known provided that the water surface is clear of surface films, which in a wind-wave tank is conveniently accomplished by blowing the films over an overflow baffle. Alternatively, if scattering measurements are made at several depression angles, the dispersion relation may be determined from the scattering measurements themselves since the Doppler shift in first-order Bragg scattering is identically the frequency of the Bragg wave. In either case the ratio of the scattered power to the square of the monochromatic wave height, measured simultaneously as a function of water-wave frequency, yields a quantity proportional to $V(k_x, 0)$. Relative values of $V(k_x, 0)$ for the Bragg wavelengths discussed here are shown in figure 2 (other examples are given by Duncan, Keller & Wright 1974). The patterns indicated by the dashed line and the one having $k_B = 1{\cdot}54\ \mathrm{cm}^{-1}$ correspond to backscattering modes using a single antenna while the other patterns were obtained with two antennae in a forward-scatter (bistatic) mode.

Proportionality between the scattered electromagnetic field and the Bragg wave amplitude is very nearly tautological for sufficiently small waves although an experimental verification has been given by Wright (1966). The diffuse scattering from the waves, however, reduces the specular reflexion coefficient by an amount proportional to the mean-square surface displacement (e.g. Valenzuela 1970). This reduces the effective mean field at the surface and so reduces the intensity of the first-order Bragg peak. The dimensionless quantity which governs this reduction is the electromagnetic roughness r, which for bistatic scattering is given by

$$r^2 = \tfrac{1}{2}(k_0 h)^2(\sin^2\theta_i + \sin^2\theta_r), \tag{4a}$$

where h is the r.m.s. surface displacement. Beard (1963, 1967) found, for forward scattering from both ocean waves and waves in tanks, that the scattered power is accurately proportional to the variance in surface displacement provided that $r^2 \leqslant 0{\cdot}2$. The scattered power deviates from this proportionality by 3 dB when $r^2 \geqslant 0{\cdot}4$. When the Bragg wave is the dominant wave (4*a*) can be rewritten as

$$r^2 = \tfrac{1}{2}(k_0/k_B)^2 s_d^2 [\sin^2\theta_i + \sin^2\theta_r], \tag{4b}$$

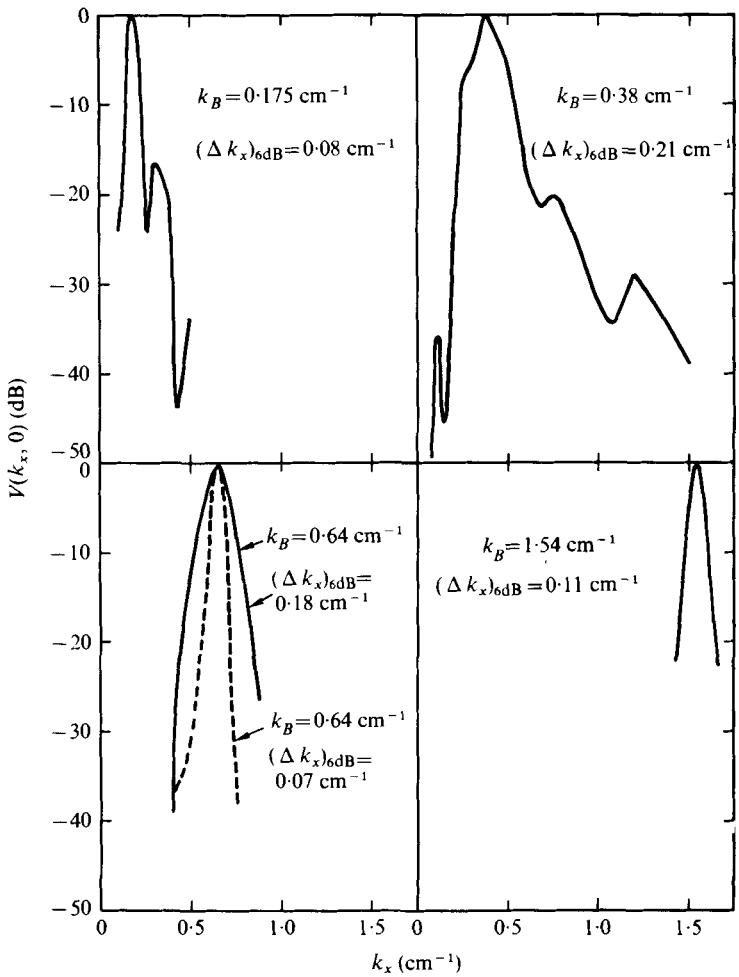

FIGURE 2. Experimentally determined antenna patterns in k space. Bragg wavenumbers k_B and wavenumber resolution Δk_x are indicated. Two different sets of scattering parameters were used for k_B = 0·64 cm^{-1}.

where s_d^2 is the mean-square slope of the dominant wave. In our tank s^2 has a maximum value of about 0·025 (Keller, Larson & Wright 1974). Thus for the scattering parameters which we used here (table 2), $2{\cdot}5 \times 10^{-3} < r^2 < 6 \times 10^{-2}$ when the Bragg wave is the dominant wave. As the dominant wave becomes longer than the Bragg wave the electromagnetic roughness increases in proportion to the dominant wavelength, if the slope of the dominant wave is constant. Thus, in the least favourable case, the criterion based on Beard's (1963, 1967) measurements is satisfied for dominant wavelengths at least twice the Bragg wavelength.

Doppler side bands, of both electromagnetic and hydrodynamic origin, occur at second order (Hasselmann 1971; Barrick 1972; Valenzuela 1974). Symmetrically placed side bands are due to the essentially free wave components of the wave system. In scattering from short gravity–capillary waves they occur at about $\pm$ 2 Hz about the first-order Bragg peak for a wide range of dominant and Bragg wave frequencies (Wright 1977). Resonant harmonic Doppler peaks of hydrodynamic origin occur, at

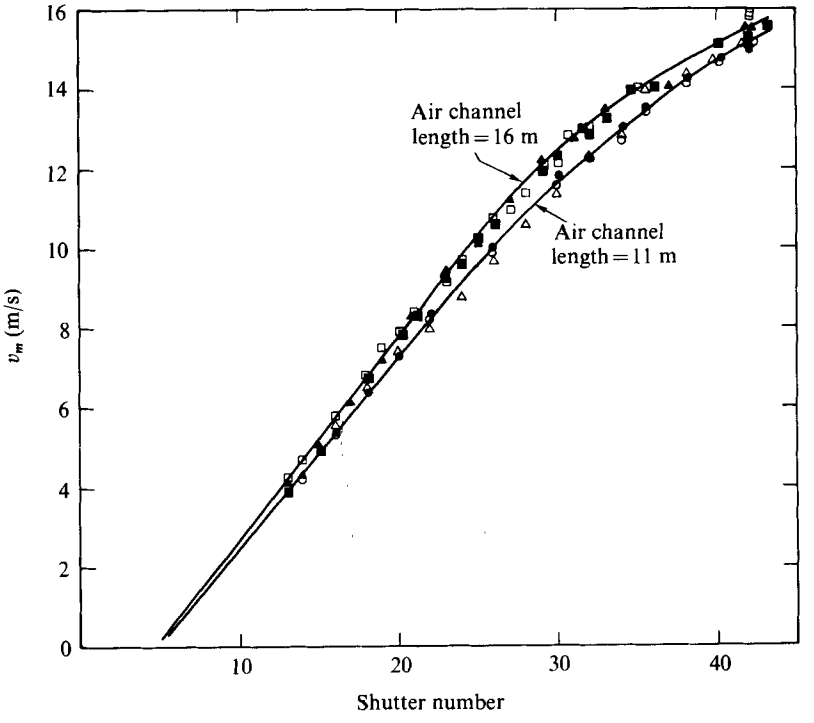

FIGURE 3. Maximum wind speed in tunnel *vs.* shutter setting at fan inlet. Fetch: ●, 0; ○, 1 m; △, 3·5 m; ■, 3·5 m; □, 7·2 m; ▲, 12·1 m.

second order and for relatively directional spectra, at twice the frequency of the wave twice as long as the Bragg wave. They may be thought of as due to bound rather than free waves. There is a similar peak of electromagnetic origin but it is not significant for depression angles of 10° or greater (Valenzuela 1974).

3. Auxiliary measurements of wind and waves

The measurements were made in the wave tank (figure 1) described by Duncan *et al.* (1974) and Larson & Wright (1975), which was, however, used in a configuration in which the total length of air channel was kept fixed and the fetch varied by exposing a variable portion of the water surface to the air flow. This facilitated precise comparison of microwave measurements at different fetches by eliminating the need for repeated boresighting of the antennae. A second feature is that the fetch is varied without changing the position at which the wind field is measured. The values of v_m, the maximum wind speed along a vertical profile at mid-channel, and u_*, the air friction velocity obtained by curve-fitting to the usual logarithmic profile

$$\overline{v(z)} = (u_*/0{\cdot}41)\ln(z/z_0), \tag{5}$$

were used to measure the mean wind. The length of air channel, except where noted, was about 35 times the air-channel height. At this distance the increment in v_m with the length of channel is small. This is demonstrated in figure 3, where values of v_m measured as a function of fetch for air-channel lengths of 11 m and 16 m are plotted *vs.*

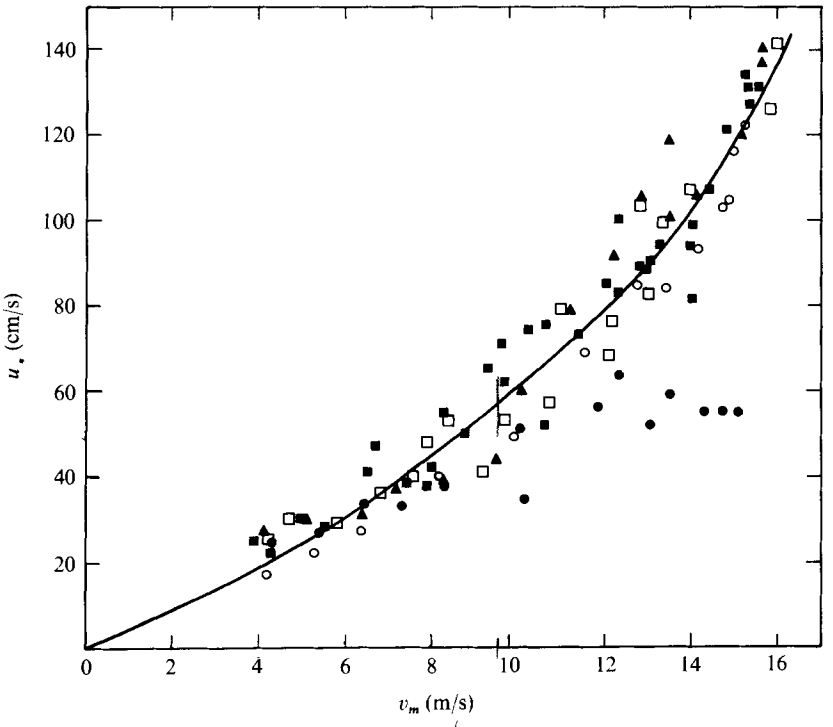

FIGURE 4. Friction velocity *vs.* maximum wind speed in tunnel. Line is empirical fit to data. Symbols as in figure 3.

the shutter number, a number denoting a calibrated setting of the position of the intake shutter on the centrifugal blower. Turbulent intensities in the free stream at the air-channel lengths were 1% and less at the high wind speeds.

Values of u_* from measurements at both air-channel lengths are plotted *vs.* v_m in figure 4. At low winds we found $u_* = 0{\cdot}05\, v_m$ in agreement with previous wave-tank work (Gottifredi & Jameson 1970). At higher winds u_* increases more rapidly than linearly with v_m, also in agreement with most wave-tank studies. An empirical fit to the data, the solid line in figure 4, is

$$u_* = 0{\cdot}02\, v_m^{\frac{3}{2}}, \tag{6}$$

which is nearly the same as the expression derived by Hidy & Plate (1966).

The dependence of u_* on fetch was measured in some detail for $v_m = 15{\cdot}5$ m/s (figure 5). The rapid increase in u_* with fetch for fetches less than 1 m may be associated with the rapid development of the wave field at high winds. The presence of spray and the greater height of waves, which prevents a sufficiently close approach to the surface, make precise values of u_* difficult to obtain at high winds and long fetches.

We previously (Larson & Wright 1975) worked at the open end of the air channel and noted that the value of u_* measured 1 m downwind of the end of the channel was as much as 10% greater than that measured at the end of the channel. In the present work a polyethylene cover 2 m long and 0·005 cm thick terminated the top of the air channel where the antennae viewed the water so that this increment in u_* was avoided.

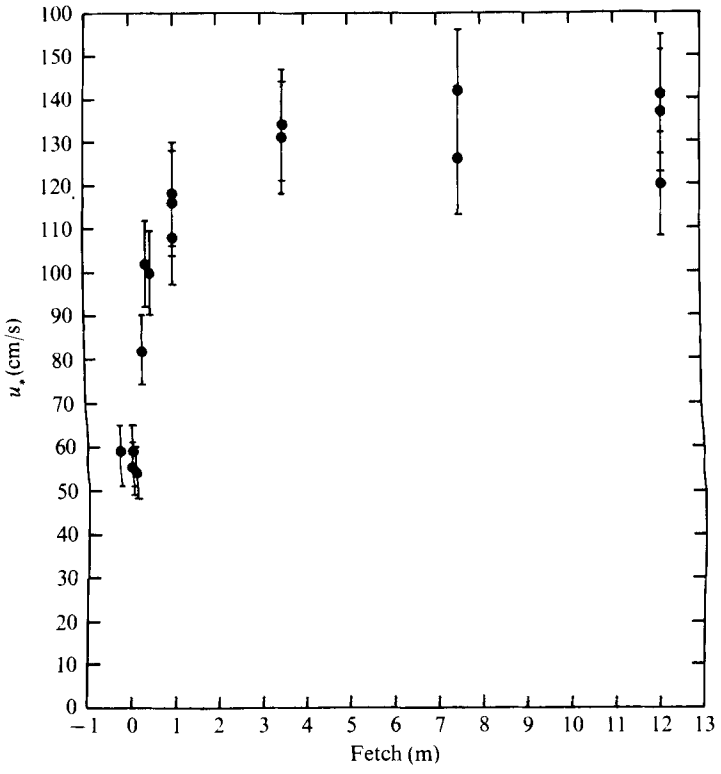

FIGURE 5. Friction velocity as a function of fetch for v_m = 15·5 m/s.

The shutter number, as it is easily and precisely measured, was the primary indicator of wind speed. The rotational frequency of the blower, measured stroboscopically, and a reference wind speed measured with a Pitot–static tube at the air-channel inlet were also recorded to ensure reproducibility of the wind speed settings. The air friction velocity, used as the measure of wind speed below, was obtained from the shutter number using the solid curve in figure 4 and the curve for an air-channel length of 11 m in figure 3. As explained previously, this procedure provided a fetch-independent measure of wind speed, but does not imply the absence of a dependence of u_* on fetch and/or axial position in the tank, such as that observed by Mitsuyasu & Honda (1975), when these are varied together. As we used the same length of air channel at all fetches, the effect of such changes tended to be minimized in our configuration. In order to isolate possible influences of beach reflexion (§5), in the case of the measurements on 16·5 cm waves, the fetch was varied by moving the antennae along the tank but the values of u_* used for these waves are those measured as described above.

A capacitance wave probe which consisted of a single strand of number 38 magnet wire was used in conjunction with the microwave measurements. This was placed in the water along with a ground wire and used as part of the input impedance of a circuit operated at 50 kHz. The frequency of the dominant wave is a convenient, single measure of the wind-generated wave field. These frequencies, obtained from spectral analysis of the capacitance-probe measurements, are shown in figure 6 as a function of

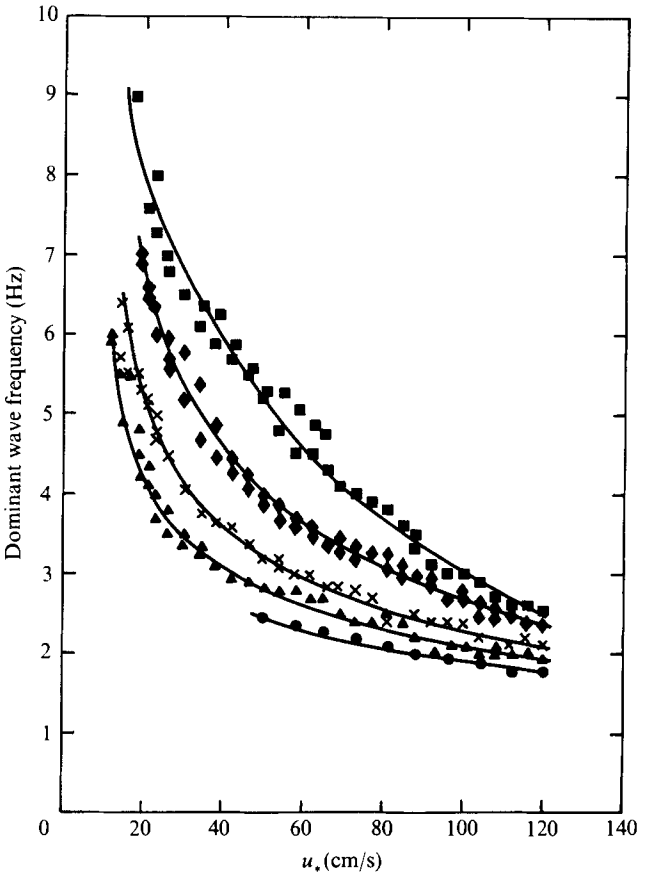

FIGURE 6. Dominant wave frequency *vs.* wind speed with the fetch as a parameter. Frequencies were taken from capacitance-probe spectra. Fetch: ●, 9·7 m; ▲, 7·5 m; ×, 5·0 m; ◆, 3·2 m; ■, 2·0 m.

Hidy & Plate (1966)		This work	
Fetch (m)	f_m(Hz)	Fetch (m)	f_m(Hz)
2·06	5·6	2·0	5·4
3·29	4·1	3·2	4·0
5·73	3·2	5·0	3·2
8·14	2·6	7·5	2·8
9·40	2·4	9·7	2·4

TABLE 1

u_* and the fetch and are compared, for $u_* = 50$ cm/s, with the measurements of Hidy & Plate (1966) in table 1. It is noteworthy that our dominant wave frequencies agree well with those of Hidy & Plate (1966) even though an exhaust fan rather than an inlet fan and a much higher wind channel were used in the latter work.

k_B(cm^{-1})	λ_B(cm)	f_0(GHz)	θ_i(deg)	θ_r(deg)	D (cm)
1·54	4·1	4·375	30	180	61
0·64	9·8	4·375	80	25	61
0·38	16·5	4·375	60	25	61
0·175	36	1·85	68	25	143
0·64	9·8	1·85	144	36	143

TABLE 2

4. Doppler spectra and their interpretation

Figure 1 shows the experimental arrangement for a bistatic condition and the microwave parameters used to observe the various Bragg waves are given in table 2. In the table, $\lambda_B = 2\pi/k_B$ is the Bragg wavelength and f_0 is the microwave frequency, while D is the antenna diameter. When $\theta_r = 180° - \theta_i$, only one antenna was used. The values given in table 2 do not quite fit (1), indicating that the antenna bore sighting did not exactly correspond to the nominal depression angles.

Examples of steady-state Doppler spectra obtained at a 8·4 m fetch and various wind speeds for 16·5 cm waves are given in figure 7. For Bragg wavelengths of 9·8, 16·5 and 36 cm, the spectral resolution was 0·2 Hz and the averaging time was 25 min; for $\lambda_B = 4{\cdot}1$ cm, the spectral resolution was 0·4 Hz and the averaging time was 12·5 min. These numbers lead to nominal 95 % confidence levels for the spectral estimates of about $\pm$ 1·0 dB. Detailed features of the spectra were generally found to be reproducible within these limits.

The Doppler frequencies shown in figure 7, i.e. the abscissae, are referred to the frequency of radar return from stationary objects. In order to avoid folding of the spectrum, this frequency was actually offset from d.c. by about 35 Hz. The figure shows that at the lowest winds both upwind- and downwind-going waves are present on the water surface and yield sharp first-order Bragg peaks at the water-wave frequency of about 3·2 Hz. As the wind speed is increased, the downwind wave grows much faster than the upwind wave until, at $u_* \simeq 34$ cm/s, it becomes the dominant wave of the system. With increasing wind speeds, higher-order lines, labelled B_2, B_3 and B_4 in the figure, appear, while the first-order Bragg line decreases in intensity. The line labelled A was consistently observed during our experiments but its origin is unknown. It does not grow as fast as the Bragg lines, however, so its presence is virtually indiscernible except at the lower wind speeds. The bump on the side of the downwind Bragg peak at $u_* = 23$ cm/s, on the other hand, is easily explainable. It occurs at the dominant wave frequency and is a result of the finite antenna patterns used in the experiments. Thus, as the Bragg wave approaches the frequency of the dominant wave, the integrand FV in (3) is nearly the same for both waves and the dominant wave is also observed.

Figures 8(*a*)–(*d*) give examples of the spectral intensity of the downwind Bragg wave as a function of u_* with the fetch as a parameter for each wavelength studied. The ordinates are the power spectral density of the Bragg line relative to the average maximum value over all fetches. These intensities were determined by simply measuring the heights of the lines, although the Bragg line spectral intensity is actually proportional to the area of the Doppler spectral peak. The line shape was always determined

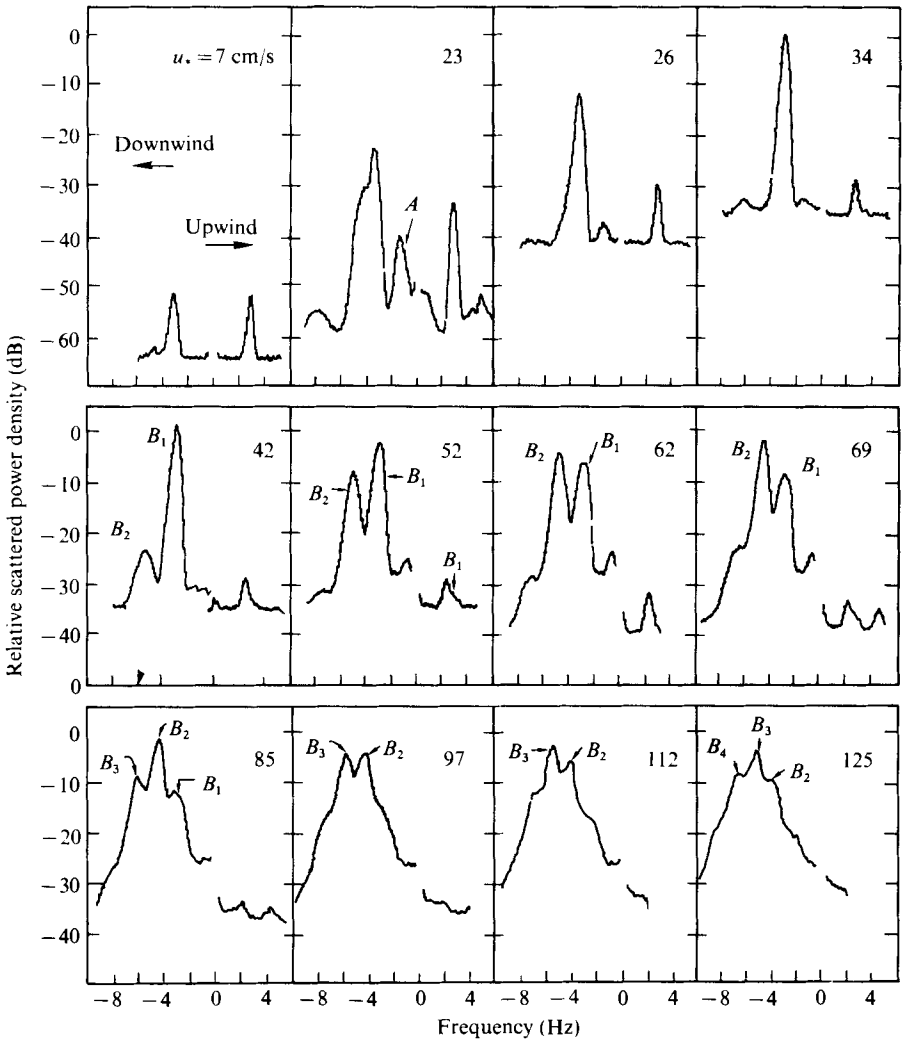

FIGURE 7. Microwave Doppler spectra of 16·5 cm waves at 8·4 m fetch for various wind speeds.

by the antenna pattern, however, so that heights and areas were proportional to each other for a given antenna arrangement. Absolute measurements of wave amplitude were obtained with a capacitance probe and/or deduced from previous slope measurements (Keller *et al.* 1974).

If the frequency of the first-order Bragg line is measured and multiplied by the Bragg wavelength, the phase speed of the water wave is determined. Phase speeds obtained in this manner for 16·5 cm waves are shown in figure 9 as a function of u_* with the fetch as a parameter. Note that the phase speeds of both upwind and downwind waves are wind-speed dependent. The speeds of the upwind waves decrease in magnitude monotonically with u_* and are not measurably dependent on fetch. For downwind waves, however, the phase speeds maximize at a wind speed which depends on fetch. Similar behaviour was observed for the other wavelengths studied. Our initial interpretation is that the upwind waves are free waves which are slowed by the

wind drift and perhaps by inertial pressure but that the downwind phase speeds are, in addition, modified by effects of finite wave amplitude. A more detailed study of the phase speeds of short gravity waves is left to the future.

The normalized first-order Bragg peak intensities for 9·8 cm Bragg waves observed with 4·35 GHz and 1·85 GHz microwave systems, respectively, are compared in figure 10(*a*). The square of the electromagnetic roughness is 5 times greater at the higher microwave frequency but the measured spectral intensities are identical, indicating that higher-order scattering effects do not significantly influence the first-order intensity. Surface displacement spectra $\psi(f, u_*)$ were obtained from capacitance-probe measurements made simultaneously with the Doppler spectral measurements at 4·35 GHz on 16·5 cm Bragg waves at a fetch of 8·4 m. Values of $\psi(f_B, u_*)/\psi_{\max}$ are seen (figure 10*b*) to be very close to the corresponding values of $P_+/P_{\max}$ as expected if the Bragg peak intensity is proportional to the spectral intensity of the Bragg wave. Note that the maximum in the probe spectra appears to occur at a slightly higher wind than that in the Bragg peak intensity; since

$$F^{-1}\left(\frac{\partial F}{\partial u_*}\right)_k \simeq c_g^{-1}\left(\frac{\partial c_g}{\partial u_*}\right)_k + \psi^{-1}\left(\frac{\partial \psi}{\partial u_*}\right)_k \tag{7}$$

this is consistent with the decrease in phase speed with increasing u_* at this fetch (figure 9). Likely contributors to the excess in $\psi(f_B, u_*)$ over P_+ at higher winds are the spatial harmonics of waves longer than the Bragg wave. Contributions from these harmonics are indistinguishable from those due to free waves in the probe spectra but harmonic contributions are excluded from the first-order Bragg peak. Since the case of 16·5 cm waves measured at 4·35 GHz was the least favourable case with respect to electromagnetic roughness it is also possible that the Bragg peak is diminished somewhat owing to the reduced reflexion coefficient at the highest winds.

Figures 8(*a*)–(*d*) show that the amplitude of a given Bragg wave, when it reaches its maximum height as u_* is varied, is nearly independent of the fetch. We examined this effect in separate series of measurements, being careful to keep all microwave settings constant. Figure 11 shows the maximum mean-square amplitudes of the Bragg waves *vs.* the wind speed at which the maximum occurs at various fetches. The absolute values of the amplitude shown in this figure were determined by integrating the capacitance-probe spectrum for $\lambda_B = 36$ cm and by optically measuring the slope when the Bragg wave is the dominant wave (Keller *et al.* 1974) for the other three wavelengths. We believe that this combination of measurements yielded the most accurate wave heights since the capacitance probe is unreliable at high frequencies and the optical method yields questionable results at wind speeds where spray is present as it is at short fetches when 36 cm waves are dominant.

The breaking of short gravity waves in the presence of wind drift has recently been treated by Banner & Phillips (1974), who showed that an oscillating, augmented wind drift occurs as the result of interaction with the orbital velocity of the wave. The augmented component of the wind drift and the drift itself increase with wind speed. Hence the wave amplitude at which the particle speed equals the phase speed decreases with increasing wind. If one uses the measured surface drift (3–4 % of the wind speed) the theory of Banner & Phillips (1974) predicts that the maximum mean-square wave height should decrease by more than 30 dB over the range of wind speeds in figure 11.

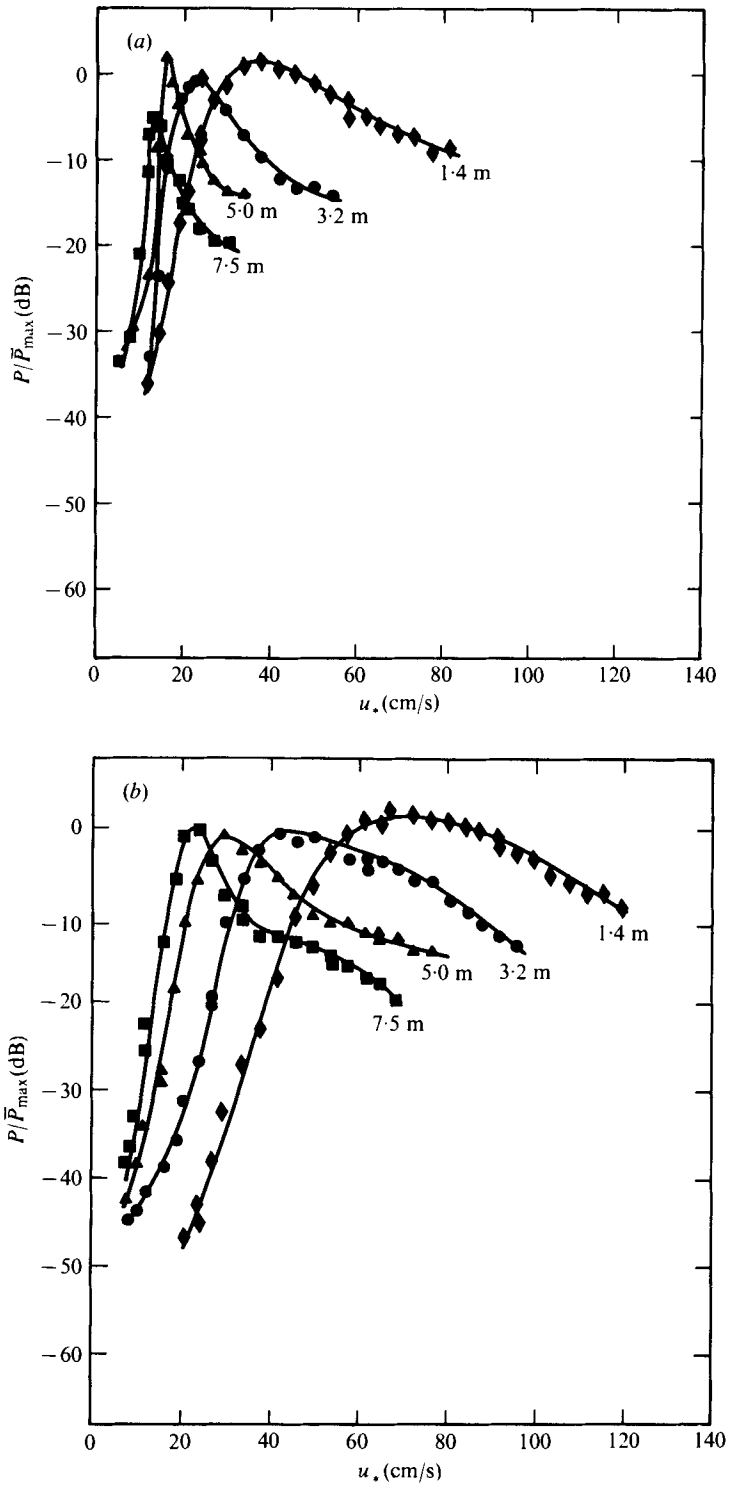

FIGURES 8 (*a*, *b*). For legend see facing page.

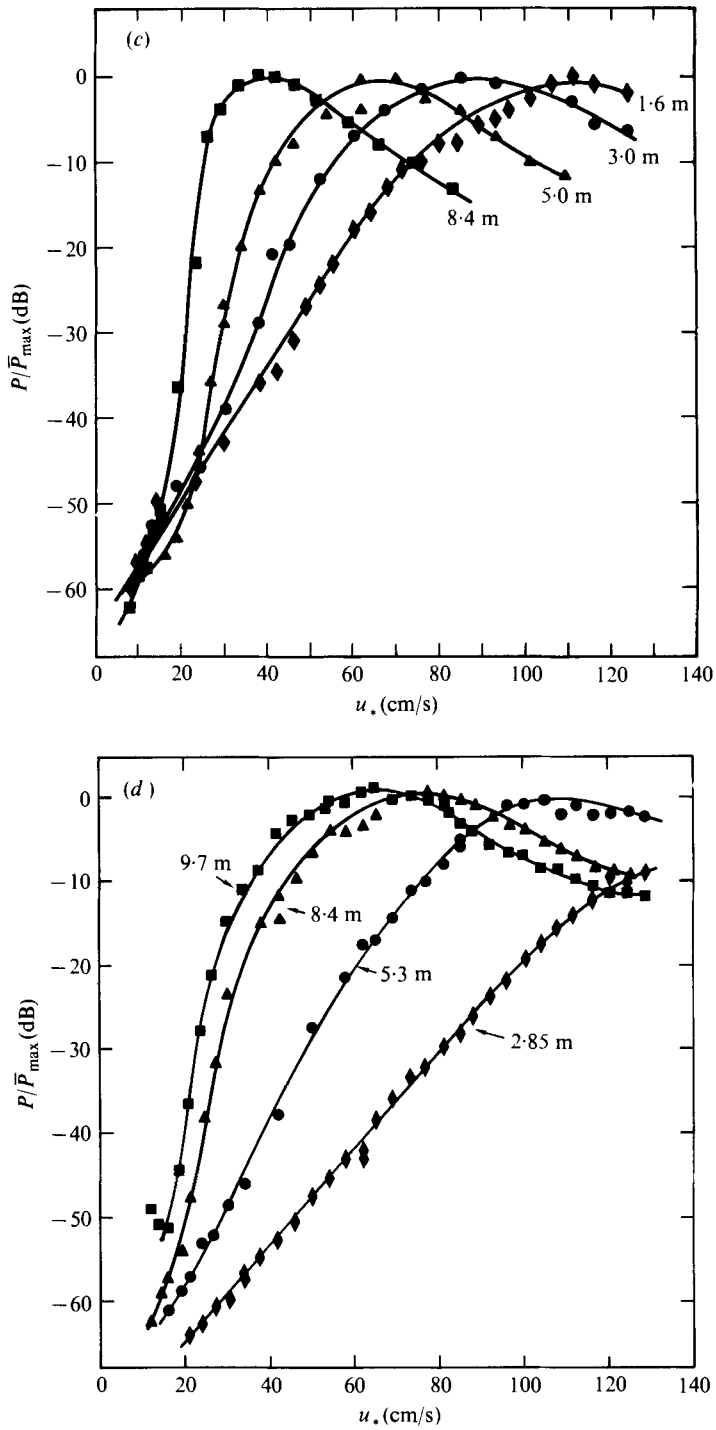

FIGURE 8. Normalized first-order Bragg peak intensity for (*a*) $\lambda_B = 4{\cdot}1$ cm, (*b*) $\lambda_B = 9{\cdot}8$ cm, (*c*) $\lambda_B = 16{\cdot}5$ cm and (*d*) $\lambda_B = 36$ cm *vs.* wind speed at various fetches. $\bar{P}_{max}$ is the average maximum power density at the various fetches.

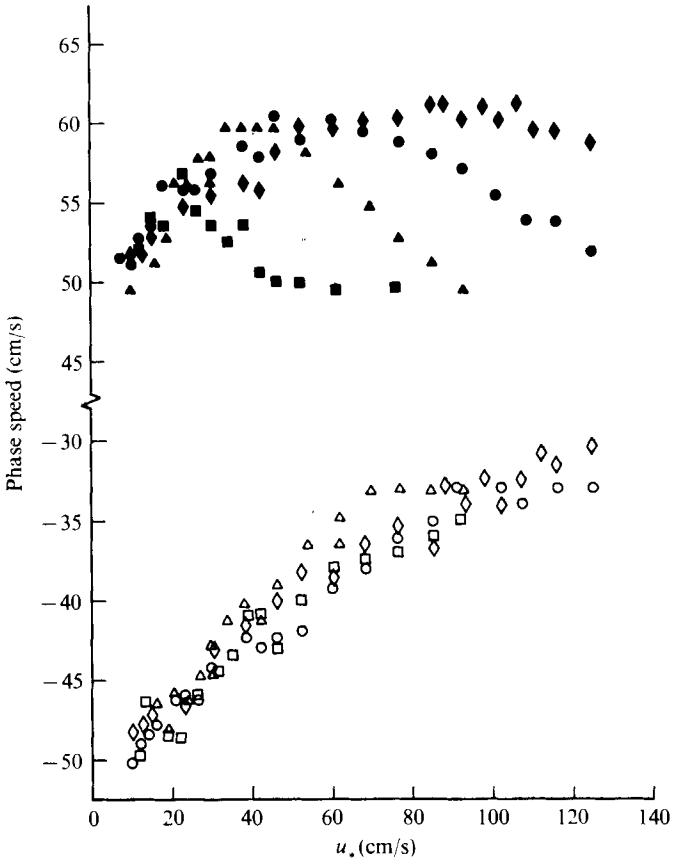

FIGURE 9. Phase speeds of 16·5 cm waves *vs.* wind speed at various fetches. Solid symbols, downwind waves; open symbols, upwind waves. Fetch: □, 8·4 m; △, 5·0 m; ○, 3·0 m; ◇, 1·6 m.

In fact, these wave heights are sensibly independent of wind speed at all four wavelengths. Thus the amplitude of short gravity waves is not limited by wave breaking induced by the wind drift (see also Wright 1976).

5. Upwind-travelling waves

The ratio of the intensities of the upwind and downwind waves is shown in figure 12. No upwind wave was observed for $\lambda_B = 4{\cdot}1$ cm. We measured the reflexion of waves in the tank without wind, due essentially to the beach, using monochromatic Bragg resonant waves: the range of reflected-to-incident ratios observed is shown in figure 12. This reflexion was much less than the maximum observed for any of the waves at low winds. Furthermore, in the case of the 16·5 cm waves, the distance from the point of observation to the beach varied from about 10·5 m at a fetch of 1·6 m to less than 4 m at a fetch of 8·4 m. Since upwind-going waves are damped by the wind the amplitude of these waves would decrease with increasing distance from the beach if beach reflexion were the cause. In fact the maximum ratio of upwind to downwind wave intensity was independent of this distance. At higher winds the ratio of upwind to downwind wave intensity was less than the beach reflexion, but at $u_* = 85$ cm/s it was necessary to

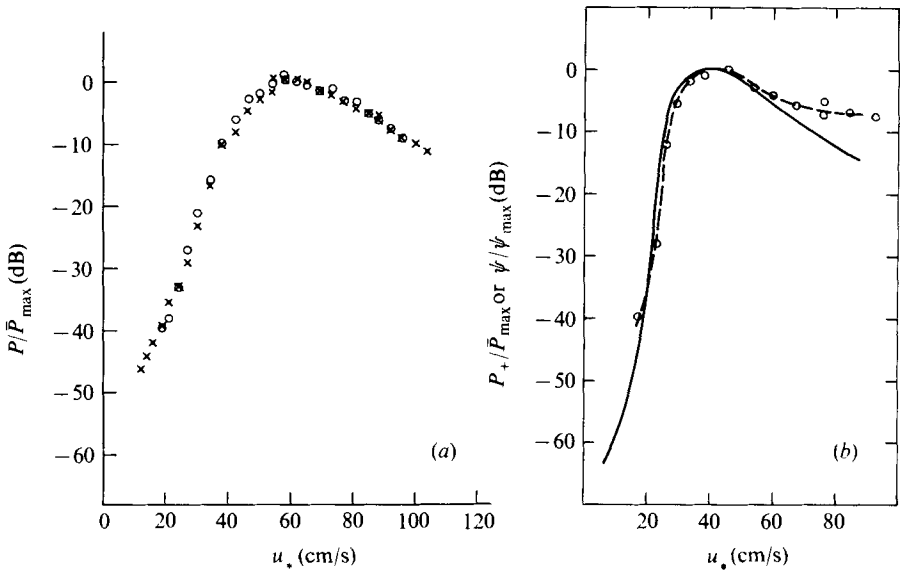

FIGURE 10. Spectral comparisons. (*a*) Normalized first-order Bragg peak intensity for λ_B = 9·8 cm *vs.* wind speed for two microwave frequencies: ×, 1·85 GHz, fetch = 2·25 m; ○, 4·375 GHz, fetch = 2·0 m. (*b*) Comparison of first-order Bragg peak intensity for λ_B = 16·5 cm (solid line) with surface displacement spectra (dashed line and circles) at 8·4 m fetch.

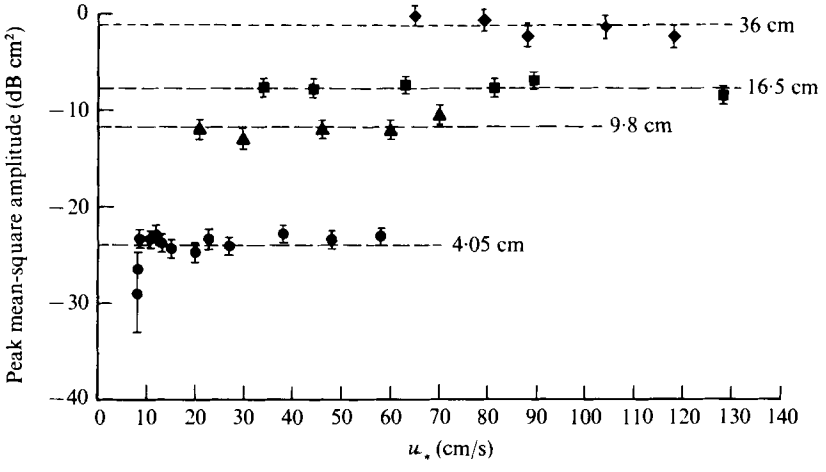

FIGURE 11. Maximum mean-square wave amplitude *vs.* the wind speed at which it occurs for various fetches.

block the waves completely with a board placed less than 1 m downwind of the illuminated area in order to produce a discernible difference in the magnitude of the upwind peak. Clearly, beach reflexion does not play a crucial role in the generation of the upwind wave.

We also made a series of measurements in which we reduced the air flow to as near zero as possible while leaving the fan running. These measurements showed that any vibration-induced 16·5 cm waves not caused by the air flow are at least 10 dB smaller than those shown in figure 7 for u_* = 7 cm/s. The upwind-going wave at light winds is thus presumably caused by interaction with the air flow. The interaction cannot, of

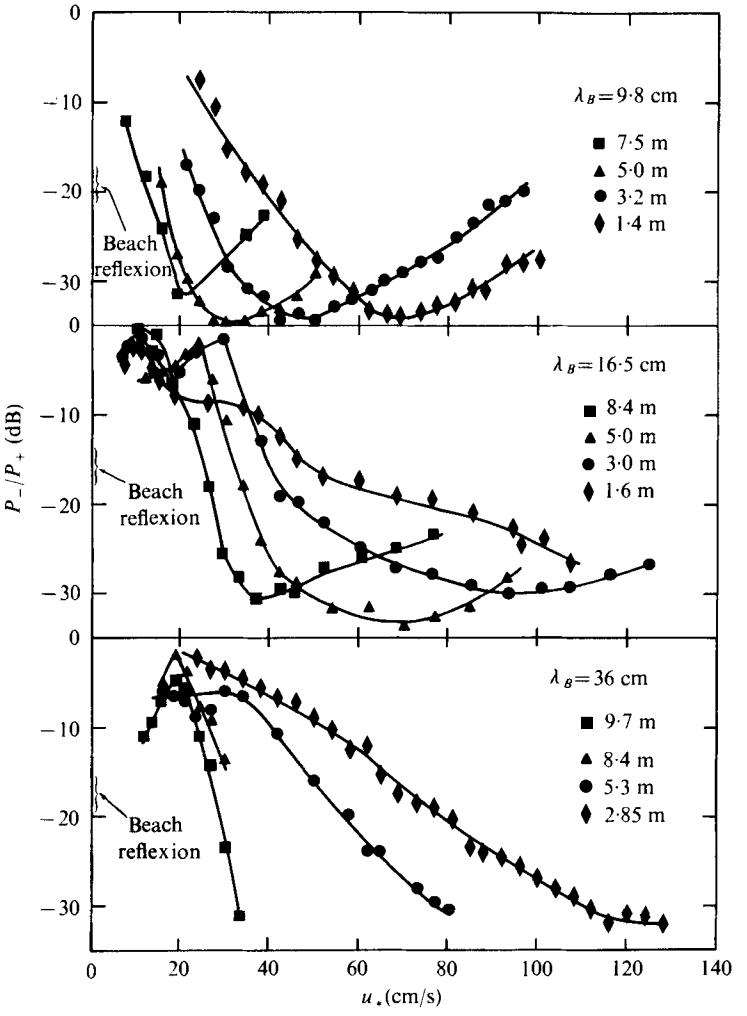

FIGURE 12. Ratio of upwind wave intensity to downwind wave intensity *vs.* wind speed at various Bragg wavelengths and fetches.

course, be a resonant interaction with turbulent fluctuations (Phillips 1957) since upwind and downwind waves are generated more or less equally. The data seem more consistent with the idea that the production of upwind waves at light winds is due to localized, non-resonant pressure disturbances.

6. Temporal growth

Temporal growth rates were measured for 9·8, 16·5 and 35 cm waves; growth rates of 4·1 cm waves were measured in an earlier study (Larson & Wright 1975). The method was similar to that used previously (Larson & Wright 1975) except that we filtered to discriminate against the dominant wave in cases when the Bragg wave was, in the steady state, longer and smaller than the dominant wave.

Measured initial growth rates for the three Bragg waves are shown in figure 13 as a function of wind speed. These data were taken at several fetches as indicated. In all

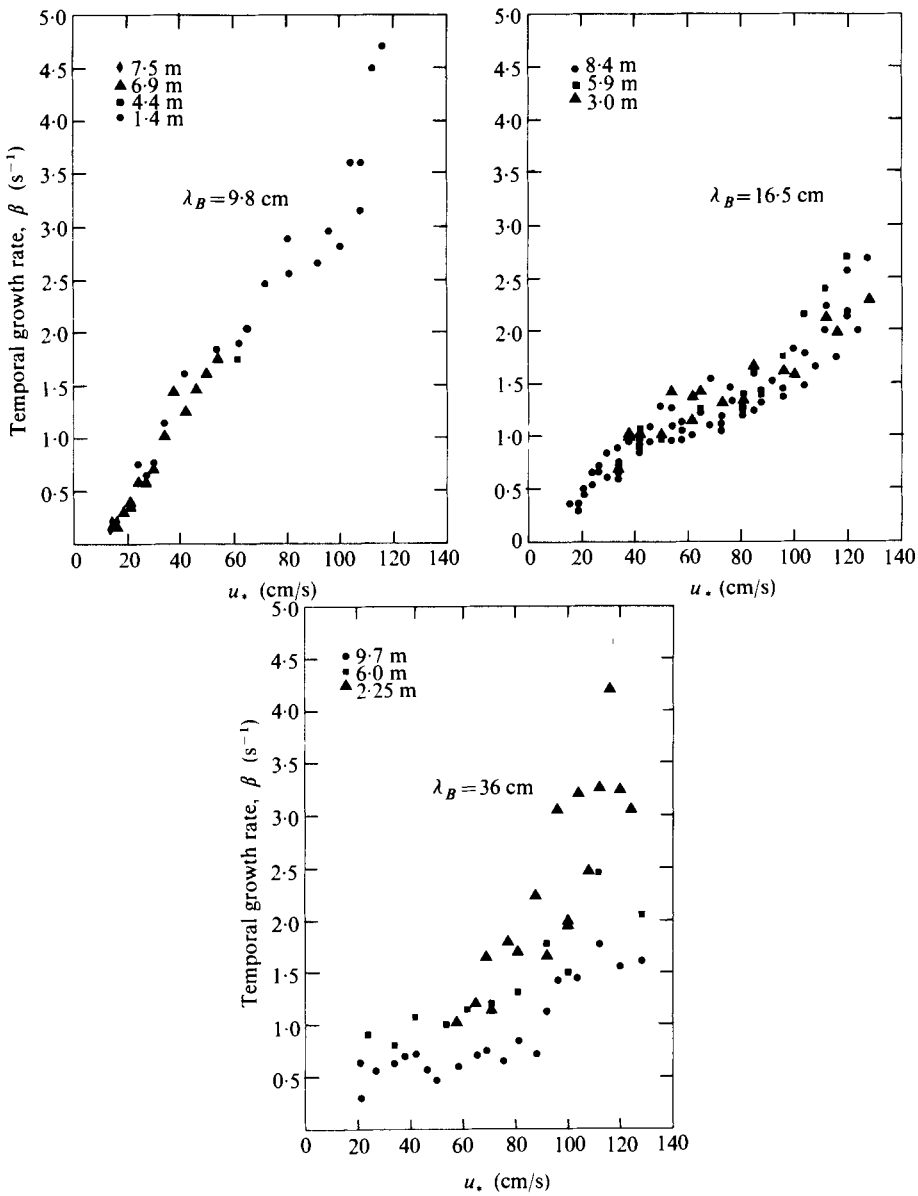

FIGURE 13. Temporal growth rates *vs.* wind speed.

cases, initial growth curves were exponential over several orders of magnitude as shown for $\lambda_B = 36$ cm in figure 14(*a*). The growth rates for $\lambda_B = 9{\cdot}8$ cm and 16·5 cm are not measurably dependent on fetch (figures 13*a*, *b*). Growth rates for $\lambda_B = 36$ cm, however, increase with decreasing fetch (figure 13*c*). This behaviour may indicate transfer from faster growing, shorter waves. Temporal growth according to such a mechanism can be qualitatively modelled by a coupled, two-wave system:

$$dF_1/dt = -\beta_1 F_1 + \alpha_{12} F_1 F_2, \tag{8a}$$

$$dF_2/dt = \beta_2 F_2 - \alpha_{12} F_1 F_2 - \alpha_{22} F_2^2. \tag{8b}$$

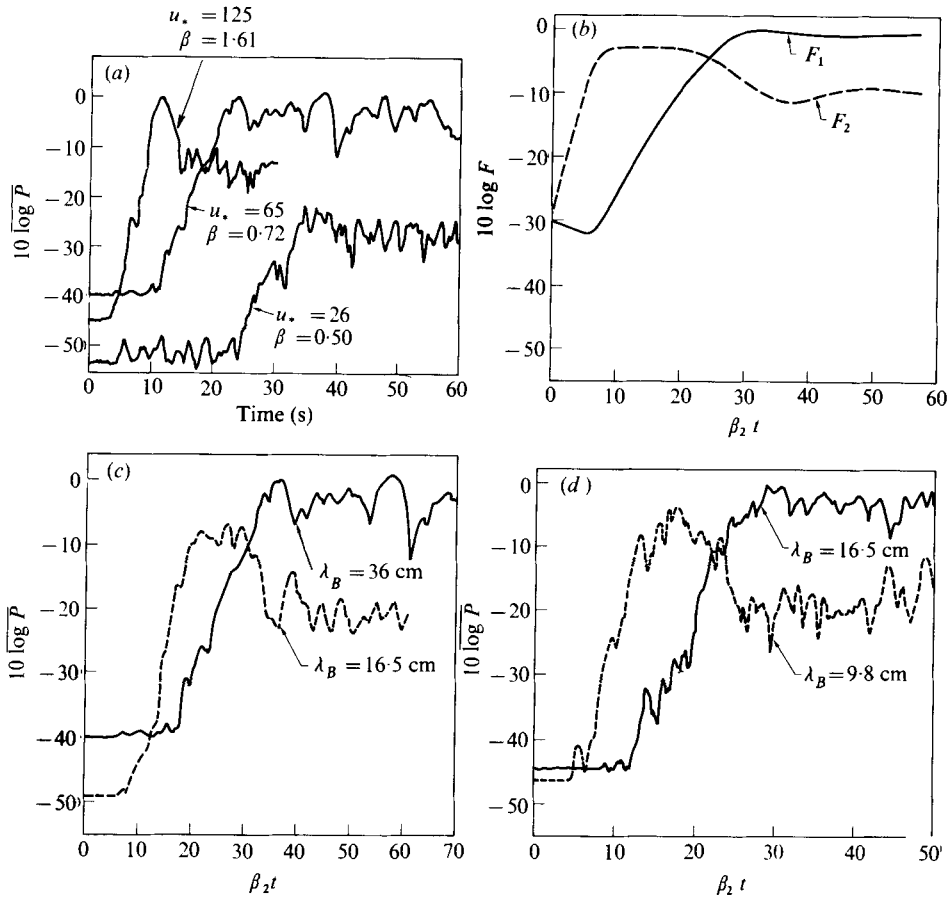

FIGURE 14. (*a*) Temporal growth curves at 9·7 m fetch for $\lambda_B = 36$ cm and various wind speeds; u_* values are in cm/s. (*b*) Computed temporal development of a two-wave system; $\beta_1 = 0{\cdot}01$, $\beta_2 = 0{\cdot}1$, $\alpha_{12} = 0{\cdot}1$, $\alpha_{22} = 0{\cdot}2$. (*c*) Temporal growth of two waves for $u_* = 65$ cm/s; fetch = 9·7 m for $\lambda_B = 36$ cm and 8·4 m for $\lambda_B = 16{\cdot}5$ cm. (*d*) Temporal growth of two waves for $u_* = 36$ cm/s; fetch = 8·4 m for $\lambda_B = 16{\cdot}5$ cm and 6·9 m for $\lambda_B = 9{\cdot}8$ cm.

The computed temporal development of this two-wave system for parameters which yield a steady-state wave F_1 about 8 dB larger than F_2 is shown in figure 14(*b*). The small negative growth rate for F_1 is an artifice introduced to stabilize the coupled system of equations; it may be thought of as a surrogate for spectral transport or transfer to yet another wave. The first point to be noted in figure 14(*b*) is that the growth of F_1 is essentially exponential even though the energy input has the form of a second-order wave–wave interaction. A number of similar calculations using growth, transfer and dissipation parameters other than those of figure 14(*b*) convince us that this is often the case. Thus the observed exponential growth over several orders of magnitude (figure 14*a*) is nonetheless consistent with growth by transfer from shorter waves. A second point is the obvious similarity of calculated curves in figure 14(*b*) to the measured histories for selected pairs of waves: 36 cm and 16·5 cm in the case of figure 14(*c*), 16·5 cm and 9·8 cm in figure 14(*d*). The abscissa in figures 14(*b*)–(*d*) is $\beta_2 t$, where β_2 is the initial growth rate of the shorter wave in each case. The pairs of histories were not

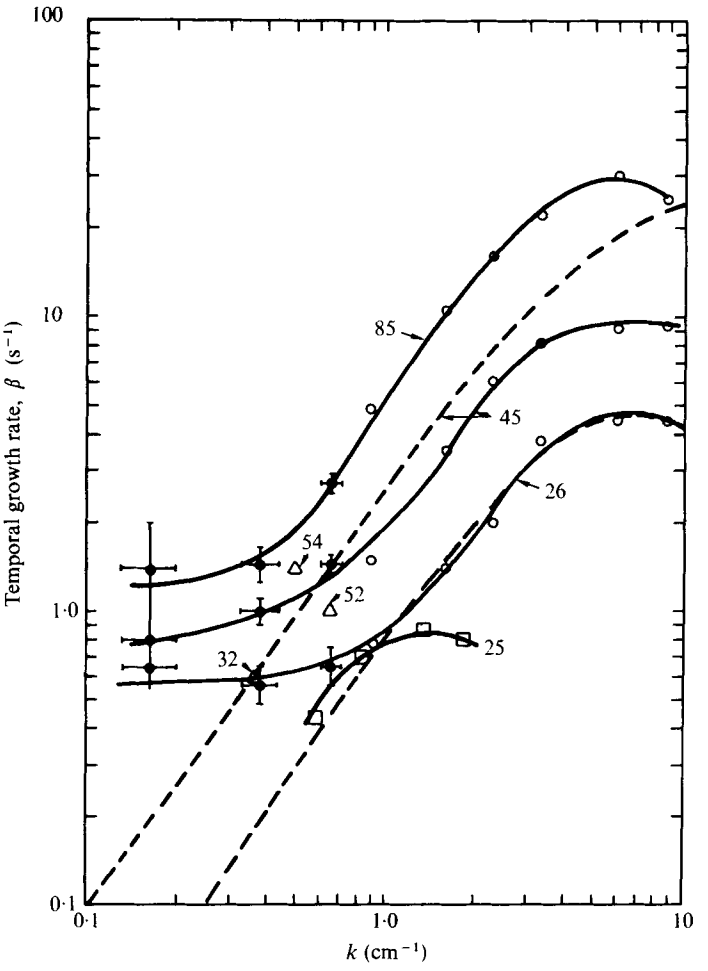

FIGURE 15. Temporal growth rates *vs.* wavenumber. Numbers indicate friction velocities in cm/s. Solid lines connect points of constant u_*, dashed lines are empirical curves. ○, Larson & Wright (1975); △, Hidy & Plate (1966); □, Gottifredi & Jameson (1970); ●, this work.

taken at exactly the same fetches but they were close enough for qualitative comparison. The relative steady-state levels in figures 14(*c*) and (*d*) are those observed in the steady-state measurements of Doppler spectra. The overshoot in the observed histories of the shorter waves could also result from a diminished influx from the wind or augmented capillary waves drawing energy away via the gravity–capillary interaction.

We compare the growth rates measured here with those obtained in other studies at similar wind speeds and wavenumbers in figure 15. The solid lines connect data points taken at the same values of u_*. The dashed lines are representations of the empirical relation

$$\beta = 0{\cdot}04u_*^2\, k/c - 4\nu k^2, \tag{9}$$

where c is the phase speed of the wave and ν is the kinematic viscosity of water. The dashed curves were obtained under the assumption of no wind-speed dependence for c.

Note that (9) fits the data taken by Larson & Wright (1975), the open circles, quite well for $u_* = 26$ cm/s. At higher wind speeds, (9) lies above the data owing to the neglect of the wind-speed dependence of c; if measured values of c are used instead, the open circles are once again well fitted. The data obtained in this study, the closed circles with error bars, fall above the curves obtained from (9), suggesting again that an additional growth mechanism, perhaps flow separation (Chang, Plate & Hidy 1971), is present for longer waves. The data of Hidy & Plate (1966), the open triangles, and those of Gottifredi & Jameson (1970), the open squares, agree well with our latest results.

Miles' (1959*a*) theory of wave growth yields the following expression for the growth rate:

$$\beta = \rho_a \xi u_*^2 \, k/\rho_w \kappa^2 c - 4\nu k^2, \tag{10}$$

where ρ_a and ρ_w are the densities of air and water, κ is von Kármán's universal turbulence constant, c is the zero-wind phase speed, and ξ is a parameter which Miles calls β. For the range of wind speeds and wavenumbers shown in figure 15, Miles finds that ξ is only slightly wind-speed dependent and has a value of about 3·3. This yields 0·027 $\times u_*^2 k/c$ for the first term in (10) in rather good agreement with the empirical relation (9) but well below the data obtained for the longer waves. For most conditions prevailing in these experiments $c < 5u_*$, so that the critical layer presumably lies within the viscous boundary layer. Thus a viscous stability theory, rather than the theory leading to (10), should be applied. However, neither Miles' (1962) nor Valenzuela's (1976) calculations extend to waves as long as 36 cm.

7. Spectral transport

The initial temporal growth of waves was observed to be exponential, as discussed above. The corresponding steady-state growth rate is the spectral transport rate $(c_g/F)\,\partial F/\partial x$, which is equal to the initial temporal growth rate if the net energy flux to the wave is the same in the steady state as in the initial temporal growth. Of course this equality will be observed only if the amplitude of the wave is small enough that the nonlinear interactions responsible for eventual equilibration of the wave are negligible. We calculated spectral transport rates from our data by plotting the spectral intensity as a function of fetch as shown in figure 16, obtaining $F^{-1}dF/dx$ from these curves and multiplying by the group speed of the waves.

Note in figure 16 that in most cases the development of these short gravity waves with fetch is exponential from inception until the wave is about 10 dB less than its maximum value. The only significant exception is the case of 16·5 cm waves at very light winds. It was shown above (figures 7 and 12) that under these conditions an upwind wave is generated which is nearly equal in amplitude to the downwind wave. This observation suggested that at light winds 16·5 cm waves are generated by localized turbulent pressure disturbances. The different generation mechanism in this case could cause the observed non-exponential fetch dependence. It is not known why this mechanism should be selectively stronger for the 16·5 cm wave than for the other wavelengths. Perhaps this is connected with the size of the eddy responsible for the turbulent generation; 16·5 cm is about one-half the height of the air channel.

The phase speed of the downwind waves depended on both wind speed and fetch in a complex and, as yet, not entirely explicable way. To retain a reasonable wind-speed

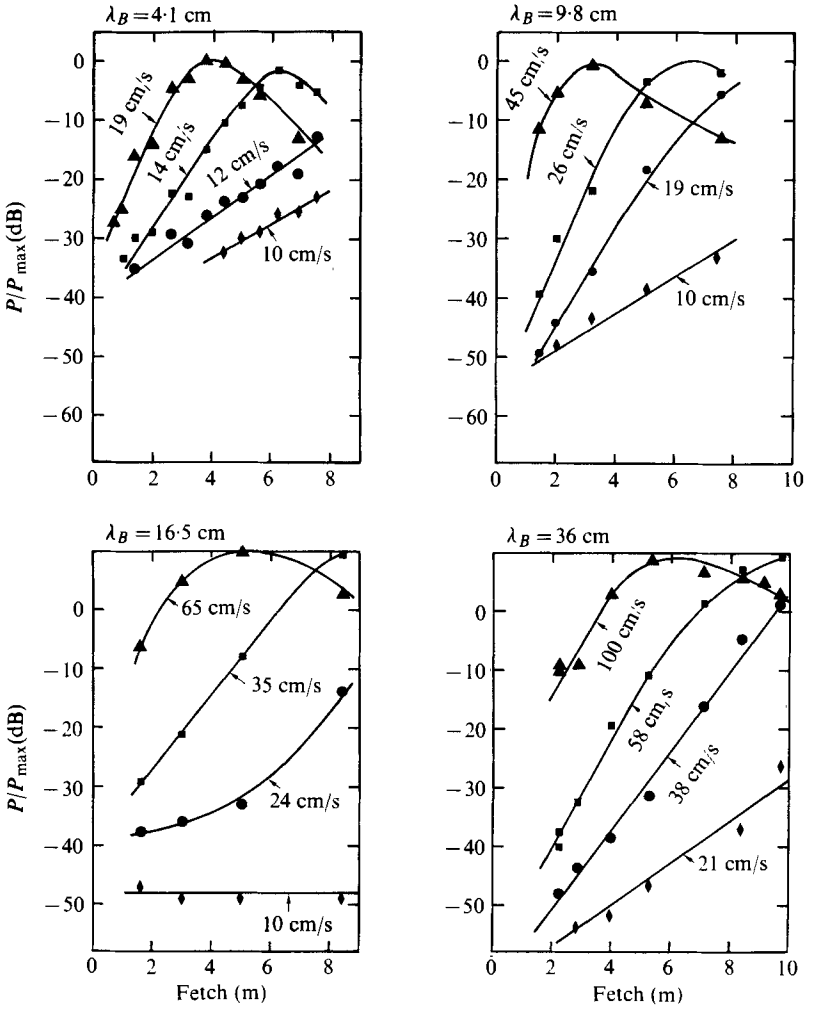

FIGURE 16. Normalized first-order Bragg peak intensity for several Bragg waves as a function of fetch at various u_* values.

dependence of the group speed for the purpose of calculating spectral transport rates we calculated the group speed using a variational method (Miles 1959*b*) and the requirement of continuity of normal stress at the air–water interface. We obtained for the radian frequency ω as a function of wind speed

$$\omega = (gk + Tk^3)^{\frac{1}{2}} + \mathbf{k}.\mathbf{U}(-0{\cdot}044\lambda), \tag{11}$$

where g is the gravitational acceleration, T is the surface tension divided by the density of water and

$$U = U_s - \left(\frac{\rho_a}{\rho_w}\right)^{\frac{1}{2}} \frac{u_*}{\kappa} \ln\left(\frac{z_0^w - z}{z_0^w}\right). \tag{12}$$

Here U_s is the surface drift and z_0^w is the roughness length in the water. Differentiating (11) with respect to k, we get

$$c_g = c_g^0 + U(-0{\cdot}044\lambda) + (\rho_a/\rho_w)^{\frac{1}{2}} u_*/\kappa, \tag{13}$$

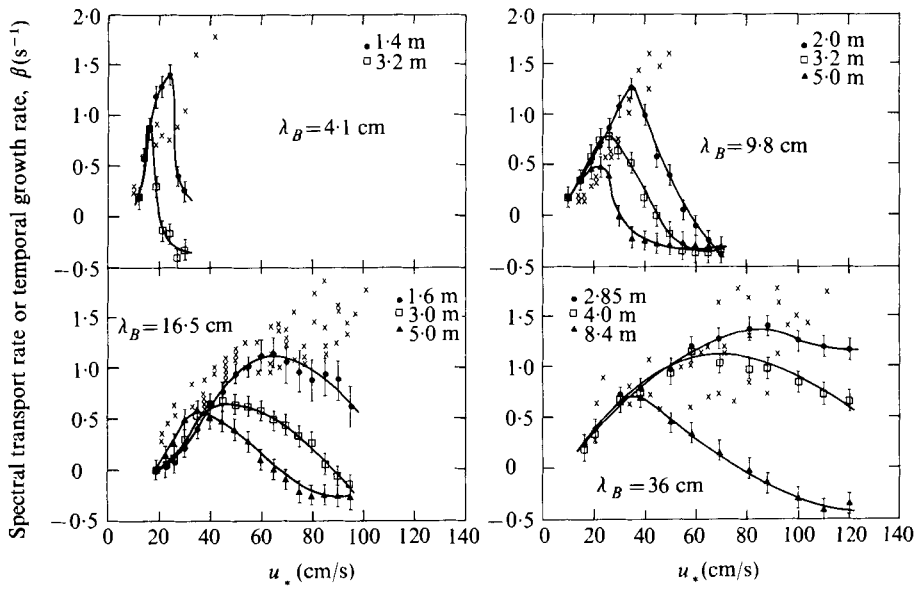

FIGURE 17. Spectral transport rates and temporal growth rates *vs.* wind speed. Data points with error bars are spectral transport rates, crosses are temporal growth rates.

where c_g^0 is the group velocity of irrotational waves. We have assumed that **U** is parallel to **k** and that $z_0^w \ll 0{\cdot}044\lambda$. Note that the wind-speed dependence of c_g is rather weak, so that if (13) is not exact, little error in the calculated spectral transport rates is expected.

Figure 17 shows the calculated spectral transport rates as a function of wind speed, with the fetch as a parameter, for the various Bragg waves. The crosses in the figure indicate measured values for the initial temporal growth rates; the values for 4·1 cm waves are from Larson & Wright (1975). The initial rise of the spectral transport rate coincides well with the measured temporal growth rates except for 16·5 cm waves at very low wind speeds, where turbulent wave generation is suspected. For friction velocities above about 30 cm/s the spectral transport rates coincide fairly well for these waves also. When the waves are small, then, the measured initial temporal growth rates are about the same as the rate of growth of the waves in the steady state.

8. Steady-state energy balance

The influx from the wind to a given wave must be balanced by transfer to other wavenumbers, dissipation or growth of the wave. The transport equation states this balance; in the case of growth along a single Cartesian co-ordinate x, along the axis of our tank, it may be written (Hasselmann 1968) as

$$\partial F/\partial t + c_g\,\partial F/\partial x = \beta F + S_{nl} + S_D, \tag{14}$$

where S_{nl} and S_D are the nonlinear transfer and dissipation respectively and we have assumed wave growth at a rate βF, as this is what we observed when the wave was small. Our results do not provide a direct measure of the energy input to a wave when it is near its maximum amplitude. However, if we assume that the energy input in the

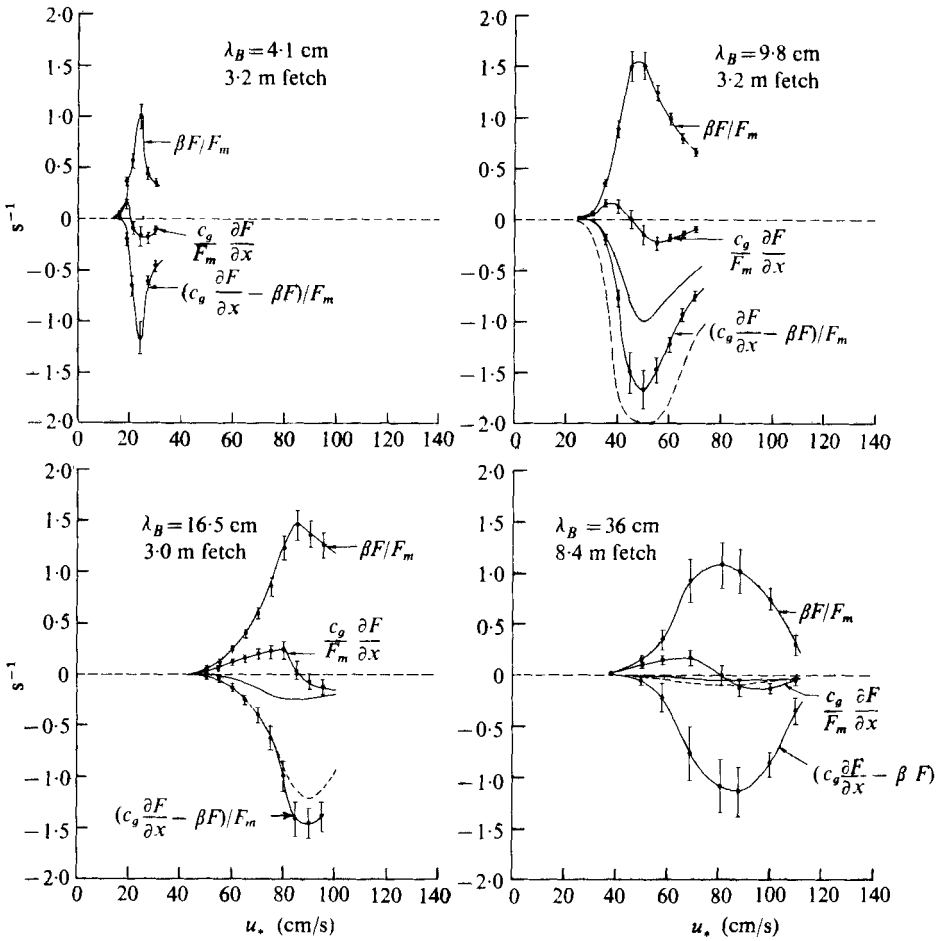

FIGURE 18. Normalized energy transfer curves. The unlabelled solid and dashed curves are values of S_{nl}/F_m calculated from second-order wave–wave interaction theory.

steady state is always given by the initial temporal growth rate, we can obtain values for $S_D + S_{nl}$ from (1). Thus, multiplying the spectral transport rate and the temporal growth rate by F/F_m, where F_m is the maximum spectral intensity, and subtracting the latter from the former yields experimental values for $(S_D + S_{nl})/F_m$ for the various Bragg waves (figure 18). In each part of figure 18, the top lines connecting data points trace the values of $\beta F/F_m$, the central lines are $(c_g/F_m)\partial F/\partial x$ and the lower curves give the difference between the other two. The spectral transport appears to be relatively small for short gravity waves whose frequencies are near that of the dominant wave. The input from the wind must be nearly locally balanced by nonlinear interactions and dissipation. Thus, though the wave system is growing with fetch, an almost local equilibrium exists for waves near the dominant wave frequency.

The assumed steady-state input to waves longer than about 10 cm is, however, too large to come directly from the wind according to the notion of Larson & Wright (1975) that short waves support the wind stress. Thus, using (9) for the influx rate and following Larson & Wright (1975), it is easy to show that the ratio of the stress supported by

the waves to the wind stress is $0{\cdot}04\,\overline{s_d^2}/(\rho_a/\rho_w)$, where $\overline{s_d^2}$ is the mean-square slope of the dominant wave. For $s_d^2 = 0{\cdot}02$ as observed (Keller *et al.* 1974), this ratio is about unity. The initial temporal growth rates for the 36 cm waves, however, exceed those given by (9) by a factor of 5 or 6 in some cases. Thus wave systems in which the 36 cm waves are dominant would, implausibly, support a stress greater than the wind stress. We infer that either the energy influx in the steady state occurs at a rate less than that of the initial temporal growth or, again, the 36 cm waves grow by transfer from shorter waves. For waves shorter than 10 cm the data give no indication of these influences on the growth rate.

Since the energy influx in the steady state is difficult to measure, theoretical determination of the nonlinear transfer would be particularly useful. The solid and dashed lines not connecting data points in figure 18 are theoretical curves of s_{nl}/F_m based on the nonlinear gravity–capillary wave interaction theory developed by Valenzuela & Laing (1972). In this theory, energy transfer occurs at second order between waves which satisfy the resonance conditions

$$\omega_1 = \omega_2 \pm \omega_3, \quad \mathbf{k}_1 = \mathbf{k}_2 \pm \mathbf{k}_3. \tag{15}$$

For the short gravity waves studied here, the minus sign applies and the resonance condition states that energy transfer from short gravity waves occurs primarily through interaction with capillary waves whose group speed is equal to the phase speed of the gravity waves. Thus, if we specialize the theory to the case where

$$k_1 \ll k_2, k_3, \quad \omega_1 \ll \omega_2, \omega_3 \quad \text{and} \quad \mathbf{U} \text{ is parallel to } \mathbf{k}$$

and assume a $Ck^{-4}\cos^2\theta$ spectrum for the capillary waves, where C is constant, we obtain

$$s_{nl} = 0{\cdot}2\,C^2 k_1^{\frac{9}{2}} - 306\,CF(k_1)\,k_1^{\frac{5}{2}}. \tag{16}$$

The solid theoretical curves in figure 18 show this result for the various Bragg waves; the value of the constant C is 0·01 as measured photometrically by Wright & Keller (1971). Since the approximations preceding (16) are not satisfied for $\lambda_B = 4{\cdot}1$ cm, no theoretical curves are shown for this wavelength, but the size of the interaction in this case can be obtained from figure 2 of Valenzuela & Laing (1972). This graph yields a value for s_{nl}/F_m of $-0{\cdot}53$ s^{-1} at the spectral peak for $\lambda = 4{\cdot}1$ cm. Thus the second-order gravity–capillary interaction yields energy transfers of the right order of magnitude but somewhat smaller than the $(s_{nl}+s_D)/F_m$ values obtained experimentally for 4·1 cm, 9·8 cm and 16·5 cm waves. The effect of the wind drift on the dispersion relation is not accounted for in (16). A result of the selectively greater advection of shorter waves by the wind drift is that the capillary waves parasitic to a given short gravity wave are longer, and hence larger, in the presence of the wind drift. This increases the strength of the second-order interaction in proportion to the increased spectral intensity of the parasitic capillary wave. We can estimate the influence of this effect by using (11) for all frequencies ω in (15). The dashed lines in figure 18 show how this modification changes the computed energy transfer, which is now large enough to match the measured values of $(c_g\,\partial F/\partial x - \beta F)/F_m$ even for 16·5 cm waves.

Although figure 18 indicates that the second-order gravity–capillary wave interaction plays an important role in the equilibration of short gravity waves of wavelengths less than about 20 cm, the possibility that other types of interaction are involved

cannot be ignored. Thus, for example, the overshoot of wave amplitude as a function of wind speed (figure 8), duration (figure 14) and fetch (figure 16) suggests the importance of other interactions. For all these overshoot phenomena, depletion of wave energy is coincident with the presence of a longer, larger wave. Perhaps a reconsideration of second-order wave–wave interactions in the presence of the wind drift would yield an analogue of the two-scale momentum transfer discussed by Valenzuela & Wright (1976). The gravity–capillary wave interaction could still play a major equilibrating role in this process as longer waves become dominant.

In any case, other interactions must become paramount at longer wavelengths where, as figure 19 and equation (16) show, the magnitude of the gravity–capillary interaction becomes small. One candidate is the third-order gravity–gravity wave interaction. We may estimate the size of this interaction for $\lambda_B = 36$ cm using the scaling relationship given by Hasselmann *et al.* (1973). Spectra in that paper were fitted to the following form:

$$F(f,\theta) = \alpha g^2 (2\pi)^{-4} f^{-5} \psi'(f/f_m, \theta), \tag{17}$$

where α is Phillips' 'constant', f_m is the peak frequency and ψ' is the shape function of the spectrum.

Thus the scaling equation given there may be written for our purposes in the form

$$s_{nl}/F_m = (2\pi)^4 \alpha^2 f_m [\psi(f/f_m)/\psi'(1,0)], \tag{18}$$

where $\psi(f/f_m)$ is a dimensionless function depending on ψ'. Spectra obtained in our wave tank were generally more peaked and had less high frequency tail than those obtained on the North Sea. If we assume, though, that the ratio in square brackets is the same in both cases and fit our spectra to the form (17), we may estimate s_{nl}/F_m at $\lambda_B = 36$ cm. We find the maximum value of the magnitude of this ratio to be approximately 10^{-3} s^{-1} for $u_* = 60$ cm/s and a 8·4 m fetch. This is to be compared with our spectral transport values from figure 18 since these are the same as the net source function given by Hasselmann *et al.* They are, in fact, the minimum energy transfers if input from the wind is entirely neglected. For the above values of u_* and the fetch the relevant value is 0·15 s^{-1}. This is one to two orders of magnitude larger than that given by the gravity–gravity wave interaction.

9. Conclusion

The nature of short gravity waves has been studied experimentally by monitoring the development of the first-order Bragg line in the microwave Doppler spectrum. We found that short gravity waves grow exponentially with time over about three orders of magnitude at rates which are higher than those suggested by capillary wave growth rates or by theory. For the longest wavelength observed, the growth rate was found to be fetch dependent, which, along with the high values of β, suggests that momentum transfer from shorter waves may be important in the initial growth of short gravity waves with wavelengths greater than about 10 cm. Spectral transport rates were found to agree with initial growth rates at small wave amplitudes, indicating that the steady-state energy influx is the same as the initial influx when the wave is small.

In the steady state, short gravity waves were found to develop exponentially with fetch in most cases until they reached a maximum amplitude at a fetch which depended

on wind speed and then to decline in amplitude at longer fetches. Similarly, the intensity of short gravity waves in the steady state increased with wind speed until it reached a maximum value at a wind speed which depended on fetch and then declined at higher wind speeds. The maximum wave height attained by a given wave was found to depend only on its wavelength. This fact indicates that wave breaking caused by an augmented wind drift is not the limiting factor in the growth of short gravity waves.

Upwind-going waves were observed at all Bragg wavelengths except 4·1 cm. At low winds the upwind waves were of the same order of magnitude as the downwind waves and, in fact, reached nearly the same height as the downwind wave for $\lambda_B = 16{\cdot}5$ cm. At low winds, the upwind waves were shown to be generated by the air flow, probably through non-resonant pressure fluctuations. The particular tank configuration used in the experiments could be the determining factor in the apparently greater generation of these waves for $\lambda_B = 16{\cdot}5$ cm than for other Bragg wavelengths.

The phase speeds of downwind waves increased with wind speed to a maximum value which depended on fetch and then decreased. The maximum phase speed occurred at lower wind speeds than the maximum wave height. Upwind waves exhibited fetch-independent phase speeds, the magnitudes of which decreased continuously with wind speed.

Short gravity waves in the neighbourhood of the dominant wave appear to exist in a local equilibrium in which the influx from the wind is nearly all locally dissipated. This is almost certainly true for waves of wavelength 10 cm or less. The second-order, gravity–capillary interaction is adequate to transfer most of the energy from waves of wavelength shorter than 15 cm to capillary waves for viscous dissipation. For longer waves, this interaction dies out and must be replaced by another, as yet unspecified, equilibrating interaction unless the rate of influx when these longer waves are dominant is very much less than the growth rate in the initial stages of growth. If this latter condition is satisfied it is also possible that a substantial portion of the influx to the 36 cm waves is advected away.

A major motivation for studying wind-generated short gravity waves is the desire to measure the energy and momentum influx from wind to waves. This is easy enough when the waves are more than 10 dB smaller than their maximum value, but in the neighbourhood of the dominant wave, the interactions which bring about equilibrium have not been extricated from the overall energy balance. A tenable hypothesis is that the system of short gravity waves grows by direct influx from the wind until it supports the wind stress, whereupon the longer waves of the system begin to grow by transfer from the shorter waves. The longest waves which grow primarily by direct influx from the air flow are probably about 10 cm in wavelength.

Preliminary measurements of temporal growth and Doppler spectra in the bistatic mode at 4·375 GHz were made by T. R. Larson. The considerable benefit which the authors derived from the results of these initial efforts is acknowledged with pleasure.

REFERENCES

Banner, M. L. & Phillips, O. M. 1974 On the incipient breaking of small scale waves. *J. Fluid Mech.* **65**, 647–657.

Barrick, D. E. 1972 Remote sensing of sea state by radar. In *Remote Sensing of the Troposphere* (ed. V. E. Derr), chap. 12, pp. 12–31. Washington: U.S. Govt. Printing Office.

BEARD, C. I. 1963 Coherent and incoherent scattering of microwaves from the ocean. *I.R.E. Trans.* AP **9**, 470–483.

BEARD, C. I. 1967 Behaviour of non-Rayleigh statistics of microwave forward scatter from a random water surface. *I.E.E.E. Trans.* AP **15**, 649–657.

CHANG, P. L., PLATE, E. J. & HIDY, G. M. 1971 Turbulent air flow over the dominant component of wind-generated water waves. *J. Fluid Mech.* **47**, 183–208.

DUNCAN, J. R., KELLER, W. C. & WRIGHT, J. W. 1974 Fetch and windspeed dependence of Doppler spectra. *Radio Sci.* **9**, 809–819.

GOTTIFREDI, J. C. & JAMESON, G. J. 1970 The growth of short waves on liquid surfaces under the action of a wind. *Proc. Roy. Soc.* A **319**, 373–397.

HASSELMANN, K. 1968 Weak interaction theory of ocean surface waves. In *Basic Developments in Fluid Mechanics*, §5.2. Academic Press.

HASSELMANN, K. 1971 Determination of ocean wave spectra from Doppler radio returns from the sea surface. *Nat. Phys. Sci.* **299**, 16–17.

HASSELMANN, K. *et al.* 1973 Measurements of wind-wave growth and swell decay. *Joint North Sea Wave Project (JONSWAP), Dtsches Hydrograph. Inst., Hamburg.*

HIDY, G. M. & PLATE, E. J. 1966 Wind action on water standing in a laboratory channel. *J. Fluid Mech.* **26**, 651–687.

KELLER, W. C., LARSON, T. R. & WRIGHT, J. W. 1974 Mean speeds of wind waves at short fetch. *Radio Sci.* **9**, 1091–1100.

LARSON, T. R. & WRIGHT, J. W. 1974 Wind wave studies. Part 2 – the parabolic antenna as a wave probe. *N.R.L. Rep.* no. 7850, pp. 1–20.

LARSON, T. R. & WRIGHT, J. W. 1975 Wind-generated gravity–capillary waves: laboratory measurements of temporal growth rates using microwave backscatter. *J. Fluid Mech.* **70**, 417–436.

MILES, J. W. 1959*a* On the generation of surface waves by shear flows. Part 2. *J. Fluid Mech.* **6**, 568–582.

MILES, J. W. 1959*b* On the generation of surface waves by shear flows. Part 3. Kelvin–Helmholtz instability. *J. Fluid Mech.* **6**, 583–598.

MILES, J. W. 1962 On the generation of surface waves by shear flows. Part 4. *J. Fluid Mech.* **13**, 433–448.

MITSUYASU, H. & HONDA, T. 1975 The high frequency spectrum of wind generated waves. *Rep. Res. Inst. Appl. Mech.* **12**, 327–355.

PHILLIPS, O. M. 1957 On the generation of waves by turbulent wind. *J. Fluid Mech.* **2**, 417–445.

VALENZUELA, G. R. 1970 The effective reflection coefficients in forward scatter from a dielectric slightly rough surface. *Proc. I.E.E.E.* **58**, 1279.

VALENZUELA, G. R. 1974 The effect of capillarity and resonant interactions on the second order Doppler spectrum of radar sea echo. *J. Geophys. Res.* **79**, 5031–5037.

VALENZUELA, G. R. 1976 The growth of gravity–capillary waves in a coupled shear flow. *J. Fluid Mech.* **76**, 229–250.

VALENZUELA, G. R. & LAING, M. B. 1972 Nonlinear energy transfer in gravity–capillary wave spectra, with applications. *J. Fluid Mech.* **54**, 507–520.

VALENZUELA, G. R. & WRIGHT, J. W. 1976 Growth of waves by modulated wind stress. *J. Geophys. Res.* **81**, 5795–5796.

WRIGHT, J. W. 1966 Backscattering from capillary waves with application to sea clutter. *I.E.E.E. Trans.* AP **14**, 749–754.

WRIGHT, J. W. 1976 The wind drift and wave breaking. *J. Phys. Ocean.* **6**, 402–405.

WRIGHT, J. W. 1977 Detection of ocean waves by microwave radar: the modulation of short gravity capillary waves. *Boundary-Layer Met.* (to appear).

WRIGHT, J. W. & KELLER, W. C. 1971 Doppler spectra in microwave scattering from wind waves. *Phys. Fluids* **14**, 466–474.